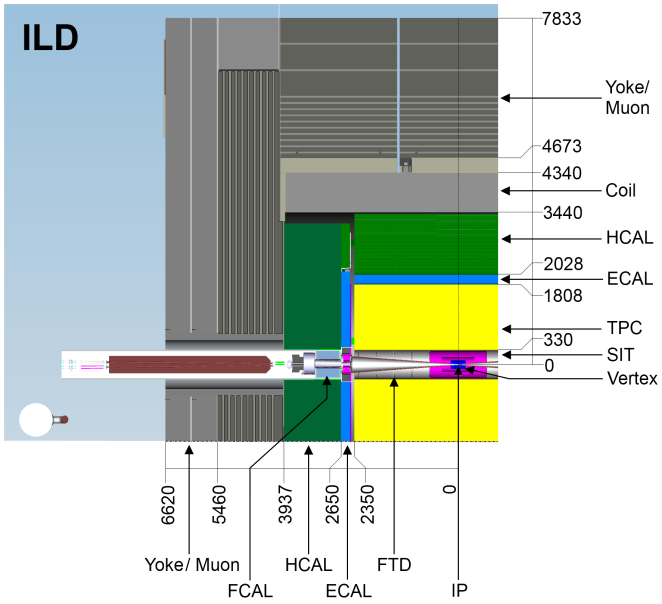

Figure 5.1. r-z structure of an ILD quadrant.

5 Detector Layout and Technologies

Claude Vallee, Karsten Buesser
1 pages

5.1 Overall structure of the detector

The geometrical structure of the ILD detector and the individual layouts of subdetectors were described in details in the ILD LOI [ref] and DBD [ref]. This section shortly reminds the main characteristics with emphasis on the recent evolutions and open options. The main design changes implemented since the DBD take into account continuous progress in detection technologies and the new optics of the ILC interaction region (chapter 3). In the following all dimensions are given for the large version of the detector (see section 4.2 for reduction factors of the small ILD).

Claude Vallee, Karsten Buesser
1 pages

5.1.1 Global structure and parameters

The overall ILD detector structure is shown in figure 5.1: a high precision vertex detector positioned very close to the interaction point is followed by a hybrid tracking layout, realised as a combination of silicon tracking with a time projection chamber, and a calorimeter system. The complete system is located inside a large solenoid providing a nominal magnetic field of 3.5T (large ILD) or 4T(small ILD) . On the outside of the coil, the iron return yoke is instrumented as a muon system and as a tail catcher calorimeter. The main geometrical parameters are summarised in table 5.1 and table 5.2.

Table 5.1. List of the main parameters of the large and small ILD detector models for the barrel part. The numbers of the inner and outer radii refer to the distance from the IP at orthogonal impact of the corresponding detector plane. The reduced radii of the small model ($\delta r = 343$ mm) are labeled with superscript^s.

Barrel system						
System	$r_{\rm in}$	$r_{\rm out}$ [mm]	$z_{\rm max}$	technology	comments	
VTX	16	60	125	silicon pixel sensors	3 double layers at $\sigma_{r\phi,z} = 3.0$ µm	$r =$ 17, 38, 59 mm (layers 1-6)
SIT	153	303	644	silicon pixel sensors	2 double layers at $\sigma_{r\phi,z} = 7.0$ µm	$r =$ 155, 301 mm (layers 1-4)
TPC	329	1770 *1427*^{s}	2350	MPGD readout	220 layers 1×6 mm^2 pads	$\sigma_{r\phi} \approx$ 60-100 µm
SET	1773 *1430*^{s}	1776 *1433*^{s}	2300	silicon strip sensors	1 double layer at $\sigma_{r\phi} = 7.0$ µm	$r =$ 1774 mm $\phi_{\rm stereo} = 7^\circ$
ECAL	1805 *1462*^{s}	2028 *1685*^{s}	2350	W absorber	30 layers	
				silicon sensor	5×5 mm^2 cells	SiECAL
				scintilator sensor	5×45 mm^2 strips	ScECAL
HCAL	2058 *1715*^{s}	3345 *3002*^{s}	2350	Fe absorber	48 layers	
				scintilator sensor, analogue	3×3 cm^2 cells	AHCAL
				RPC gas sensor, semi-digital	1×1 cm^2 cells	SDHCAL
Coil	3425 *3082*^{s}	4175 *3832*^{s}	3872		3.5 T field	int.lengths $= 2\lambda$
Muon	4450 *4107*^{s}	7755 *7412*^{s}	4047	scintillator sensor	14 layers 3×3 cm^2 cells	

Table 5.2. List of the main parameters of the large and small ILD detector models for the end cap part. The numbers of the inner and outer radii refer to the distance from the IP at orthogonal impact of the corresponding detector plane. The reduced radii of the small model are labeled with superscript ^{s}.

End cap system							
System	z_{min}	z_{max}	r_{in}	r_{out}	technology	comments	
		[mm]					
FTD	220 645	371 2212		153 300	silicon pixel sensors silicon strip sensors	2 discs 5 double discs	$\sigma_{r\phi,z} = 3.0$ µm $\sigma_{r\phi} = 7.0$ µm $\phi_{\mathrm{stereo}} = 7\,^\circ$
ECAL	2411	2635	250	2096 *1718*^{s}	W absorber	30 layers	incl. EcalPlug
					silicon sensor	5×5 mm^2 cells	SiECAL
					scintilator sensor	5×45 mm^2 strips	ScECAL
HCAL	2650	3937	350	3226 *2876*^{s}	Fe absorber	48 layers	
					scintilator sensor, analogue	3×3 cm^2 cells	AHCAL
					RPC gas sensor, semi-digital	1×1 cm^2 cells	SDHCAL
Muon	4072	6712	350	7716 *7366*^{s}	scintillator sensor	12 layers 3×3 cm^2 cells	
BeamCal	3115	3315	18	140	W absorber GaAs readout	30 layers	
Lumical	2412	2541	84	194	W absorber silicon sensor	30 layers	
LHCAL	2680	3160	130	315	W absorber		

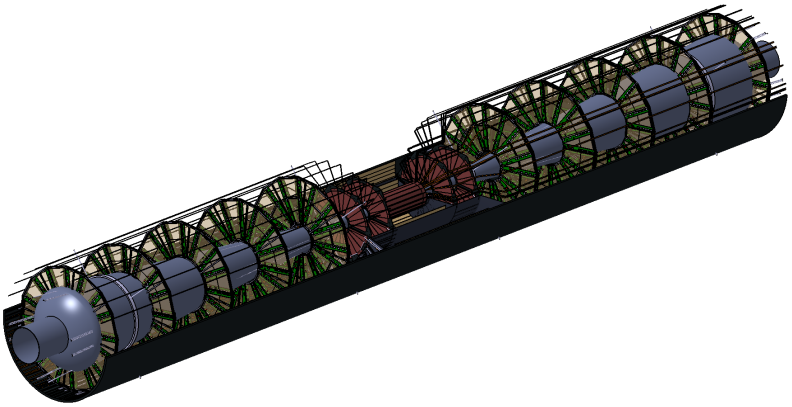

Figure 5.4. layout of the Forward Tracking Detector.

with the r-coordinate is less constrained. These requirements can be met with micro-strip detectors: two single-sided detector mounted under a small stereo angle may provide the required resolution. A solution based on CMOS monolithic pixel detectors with elongated pixels is likely to be quite competitive. Also the possibility o.f a Time-Of-Flight measurement in the outermost disks merits further study.

TPC *(Colas, Sugiyama)*

A distinct feature of ILD is a large volume time projection chamber (Figure 5.5 left). The TPC allows a continuous 3-dimensional tracking, dE/dx-based particle identification and minimum material. The required performance of the TPC as a standalone tracker is a momentum resolution $\delta(1/P_T)$ better than $10^{-4}GeV^{-1}$, corresponding to a single point resolution of 100μ over about 200 points, and a dE/dx resolution better than 5%. One critical issue concerns potential field distortions due to ion accumulation within the chamber. At ILC this can be mitigated by implementing an ion gating between bunch trains: ions produced in the gas amplification region during bunch trains are confined and eliminated outside bunch trains by reverting the electric field configuration. This can be implemented with GEM foils as shown in Figure 5.5 right.

Three options are under consideration for the ionisation signal amplification and readout:

- GEM readout (Figure 5.6 left): the ionisation signal is amplified by passing through a GEM foil and is collected on pads.
- Micromegas readout (Figure 5.6 right): the ionisation signal is amplified between a mesh and the pad array where it is collected.
- GridPix: the ionisation signal is amplified as for the Micromegas case but collected on a fine silicon pixel grid providing individual pixel timing.

For the GEM and Micromegas options, the typical pad sizes are a few mm (table 5.1) and spatial resolution is improved by combining the track signals of several adjacent pads. For the GridPix option the pixel size of ≈50 microns matches the size of the mesh, providing pixel sensitivity to single ionisation electrons. The spatial resolution is improved and the dE/dx signal is measured by counting pixels or clusters.

ECAL *(Brient, Ootani)*

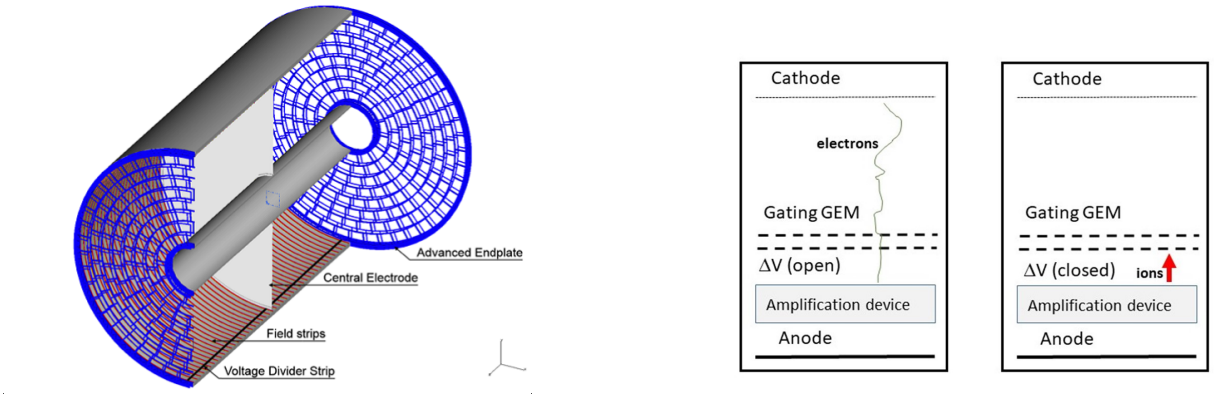

Figure 5.5. Left: Global layout of the TPC chamber. Right: Principle of the ion GEM gating scheme showing the two electric field configurations within (left) and outside (right) bunch trains.

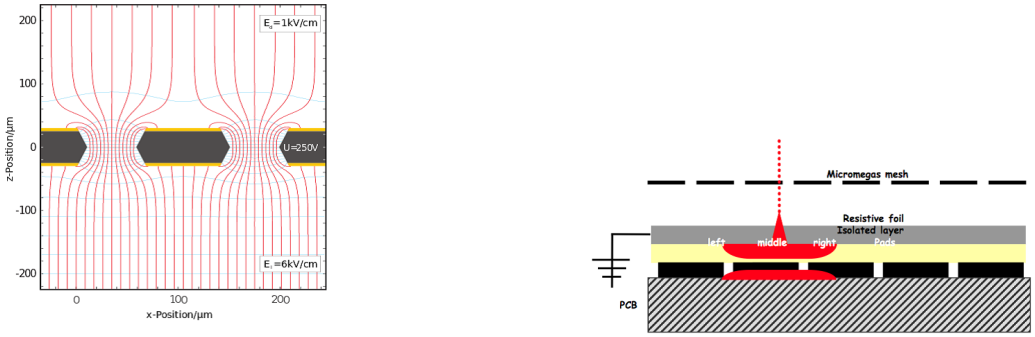

Figure 5.6. Amplification scheme of the TPC ionisation signals with GEM (left) and Micromegas (right) readout.

Electromagnetic showers are measured with a compact highly-segmented calorimeter (Figure 5.7) which absorber planes are made of tungsten. The ECAL barrel shape is octagonal with individual stacks laid such as to avoid projective dead zones in azimuth. The baseline number of layers is 30, with options to reduce the number to 26 or even 22, keeping the amount of radiation lengths identical and increasing the thickness of the sensitive medium to maintain a similar energy resolution.

The sensitive medium consists in silicon sensors with about 5x5 mm^2 pads bonded on a PCB equipped with front-end readout ASICs (Figure 5.8 left). In order to reduce the costs it is considered to equip part of the sensitive layers with scintillator sensors readout through SiPMs (Figure 5.8 right). In that case the scintillator strips would have a larger dimension of 45x5mm^2 with alternate orthogonal orientation. The option to equip the first layer with high-resolution timing sensors is also under consideration to provide a TOF functionality.

HCAL *(Laktineh, Sefkow)*

The hadronic calorimeter consists in 48 longitudinal samples with steel absorber plates. Two

5.2 Subdetector technology status

All ILD detector technologies under consideration have benefited from substantial developments since the DBD publication. Many activities are coordinated within worldwide R&D Collaborations such as LCTPC [ref], CALICE [ref] or FCAL [ref]. Compared to the DBD studies, which were still focused on intrinsic physics response and performance, many technologies have now developed operational implementations with technological prototypes which are mature for extrapolation to a full detector. Applications have indeed already started with many spin-offs to existing experiments such as the high-luminosity LHC detector upgrades. The experience gained with these projects will be a strong asset to the final design and construction of ILD.

Auguste Besson, Akimasa Ishikawa, Marcel Vos
3 pages

5.2.1 Vertex detector

The vertex detector is a high-precision small device which is expected to be one of the latest subdetectors to be built and inserted within ILD. The development of optimal technologies can therefore proceed until a few years before the start of ILC. There has been much progress in this direction in the past 5 years for the three main options under consideration: CMOS, DEPFET and FPCCD sensors.

CMOS sensors: The use of CMOS sensors for particle physics has benefited a lot from the development in the past two decades of the MIMOSA chip series by the IPHC Institute [ref]. A first full scale particle physics detector application has been realized with the STAR vertex detector (Figure 5.14) on the RHIC hadron collider. Since then the technology has further developed as a widespread standard for pixel detectors, including many applications to e.g. LHC upgrades or new experiments.

The general trend of performance improvements towards ILD specifications is summarized in table 5.3. Compared to STAR the new applications for the ALICE upgrade and CBM at FAIR have moved to a technology with a smaller pattern, have implemented a new data driven readout scheme, and have improved the time resolution and power consumption to values close to ILD needs. The ALICE detector also concerns a very large area of more than 10 m^2, which qualifies the technology for the inner layers of a central tracker.

With these applications more attention is given to integration aspects of the technology. The chip intrinsic power consumption is now close to the ILD specification and could still be reduced by a factor $\simeq 10$ with power pulsing. To this respect a trade-off will have to be made between readout speed (related to time resolution) and power. With the expected heat production air cooling as done at STAR could be sufficient, but ILD has stronger constraints on the possible air flow due to a more forward instrumentation than STAR. This critical issue requires further studies. Low material ladder supports have been developed with the "PLUME" concept, consisting in a thin foam layer carrying pixel chips on both sides as a double layer [ref]. First PLUME ladders have been built and a second version has been successfully operated for the BELLE II beam commissioning (Figure 5.15 top).

DEPFET sensors: The development of DEPFET sensors in particle physics is reaching maturity. Following the demonstration of small prototypes [16, 17] and first operational ladders five years ago the technology was chosen as the baseline for the vertex detector [18] of the Belle II experiment [19]. As many requirements of Belle II are similar to those of the ILC, this can be seen as a 30% prototype of the ILC vertex detector. DEPFET ladders have been successfully used in the BELLE II beam

Table 5.4. Contribution to the material bugdet of the Forward Tracking Disks. The contributions are determined for perpendicular incidence and average over the area of the disk.

Component	material (% X_0)
Silicon petals	
Carbon fibre (incl. cyano-ester resin)	0.038
Honeycomb core (Aramide)	0.0006
PEEK inserts	0.0019
PEEK screws	0.0014
glue	0.0006
total	

of the experiment (Figure 5.19). This *mock-up* is based on a Carbon-fibre support disk and 50 μm thick silicon petals designed at IFIC Valencia.

The Carbon fibre disks were produced by INTA in Madrid. It consists of a 1 mm thick rohacell core covered on both sides by three-layer carbon fibre skins. The resulting structure adds less than XXX % of a radiation length (X_0) to the material budget. The mounting points for the Silicon sensors are formed by precisely machined PEEK inserts that are glued into the Carbon fibre structure. The gluing procedure controls the relative position of the mounting points to better than 50 μm with a custom jig.

The Silicon petals were produced at the HalbLeiterLabor of the Max Planck Society in Munich (MPG-HLL) using the Silicon-on-Oxide process that is at the heart of the all-silicon-ladder concept [15]. The 50 μm thick sensor area is supported by a 500 μm thick rim.

The contribution to the material budget of the sensors and support disks is summarized in Table 5.4. The Silicon sensors clearly dominate the total contribution.

The thermo-mechanical performance of the loaded disk has been tested extensively. The support disk is found to have a planarity of 200 μm (RMS). Despite the minimal material it is very stiff, with an eigenfrequency greater than 1 kHZ. The silicon petals are mounted kinematically, such that are free to expand in response to a thermal load, while distortions of the sensors out of the nominal plane remain very tightly constrained. The torque applied to the screws must be carefully chosen: a torque of 3 $mN \cdot m$ is found to be optimal. With this choice, the first eigenfrequency of a free petal (167 Hz) is nearly doubled (to $\sim$ 270 Hz) when the sensor is clamped to the disk

The impact of air cooling on the mechanical stability is studied with a local, laminar air flow. The power consumption pattern mimics that of a DEPFET active pixel detector, assuming that the application of power pulsing reduces the average power consumption by a factor 20. In these conditions, a gentle, laminar flow of 1 $\mathrm{m/s}$ is found to be sufficient to keep the temperature gradient over the sensor to within 10 degrees C, Vibrations due to air flow have an amplitude of less than 1 μm for laminar air flow with a velocity up to 4 $\mathrm{m/s}$.

These results indicate that an aggressive design based on a thin Carbon fibre support disk and ultra-thin self-supporting Silicon petals can meet the stringent requirements on mechanical stability of the ILD experiment.

Paul Colas, Akira Sugiyama
3 pages

5.2.3 Time projection chamber

The ILD TPC R&D is being conducted mainly within the LCTPC Collaboration [23].

The workhorse for validation of detector prototypes and operational conditions is the TPC test set-up installed permanently in the DESY test beam [24] (Figure 5.20). The TPC stands within a magnet providing a magnetic field of 1 Tesla, and the beam line is equipped with precise incident and

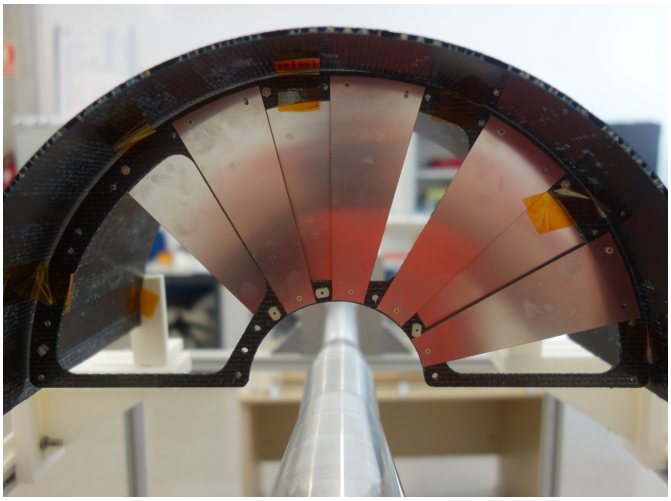

Figure 5.19. FTD thermo-mechanical mockup for the 2 inner disks.

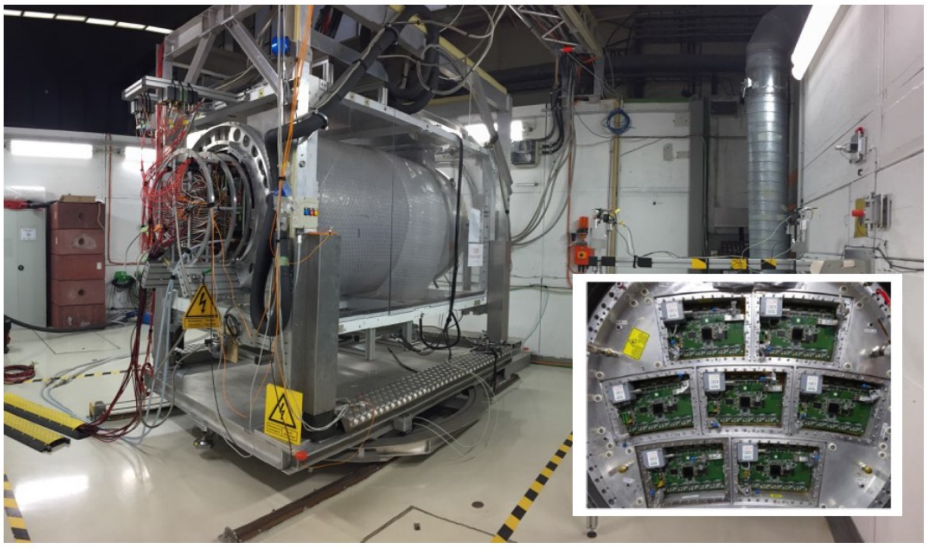

Figure 5.20. The TPC test setup at DESY. The insert shows the geometrical structure of the TPC end cap which can host prototypes of detection planes.

outgoing particle beam telescopes allowing to quantify the TPC reconstruction precision as function of the particle parameters. The beam test set up is currently being upgraded with the high precision LYCORIS silicon telescope [25], and a new TPC field cage with reduced field distortion is being assembled.

Significant progress has been seen in the manufacturing process of detection modules for each of the readout options. A new micromegas layout with resistive anodes has been shown to exhibit reduced boundary distortions [26]. The flatness of the GEM modules has been improved significantly, increasing the gain uniformity by a factor 2 [ref]. Operational GridPix "QUAD" modules have been built based on the TimePix3 pixel chip [27]. Recent prototypes of the three types of detection modules are shown in Figure 5.21.

The performance of the three technologies has been measured in beam tests. Figure 5.22 shows the measured point resolution in 1 T magnetic field for drift distances from 0 to 0.6 m. This can be safely extrapolated to $\sim$ 100 μm in a field of 3.5 T at a drift length of 2.3 m. The dE/dx resolution by the truncated mean method has been measured to be respectively $4.6\%, 4.5\%$ and 4.2%

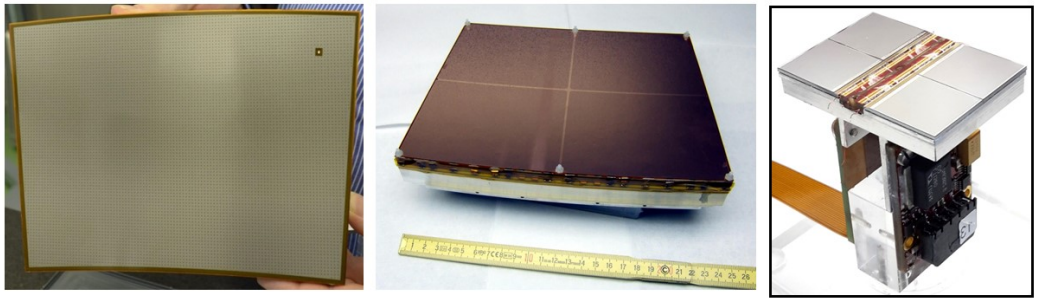

Figure 5.21. TPC prototype detection modules for the three baseline technologies under consideration: micromegas module (left), GEM module (middle) and GridPix QUAD module (right).

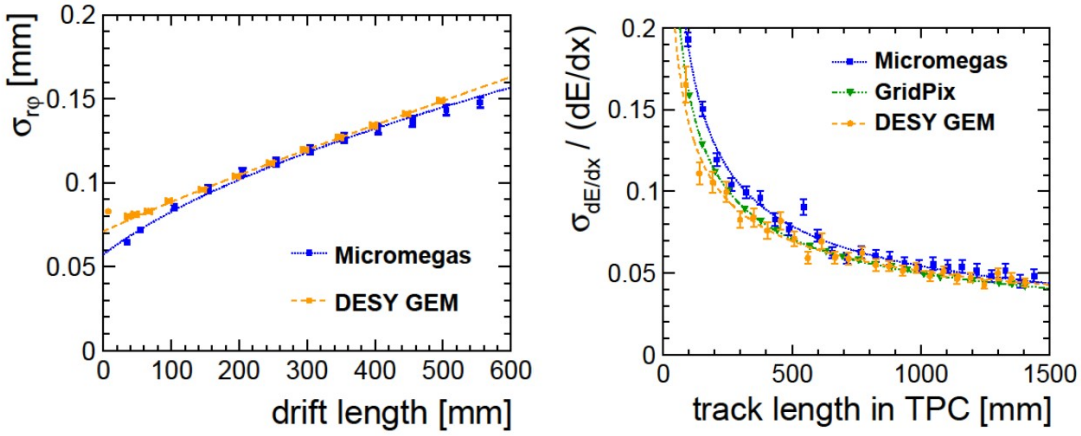

Figure 5.22. Resolution on the track position in rϕ (left) as function of the drift length and resolution on the ionisation loss dE/dx (right) as function of the track length, for the three readout options under consideration.

for Micromegas, GEM and GridPix technologies. It improves to 3.8% for GridPix using a cluster counting method. The conclusion is that the target goals of a spatial resolution of 100 microns and of a dE/dx resolution better than 5% have been reached in all cases.

Q: add performance plot of 2 track separation?

Two critical aspects of a TPC operation consist in the cooling of the readout endcaps, which must be realized with minimal dead material, and the mitigation of the drift field distortions which may develop from the accumulation of ions in the drift volume. For the first point a double phase CO_2 cooling system with thin low-material fluid pipes has been developed and shown to perform

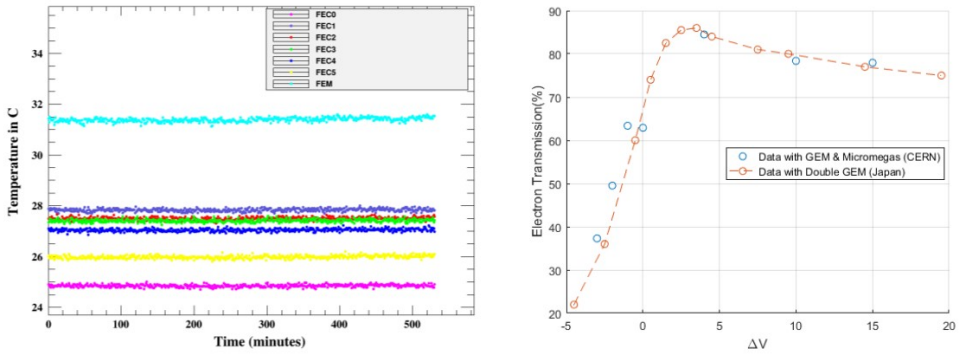

Figure 5.23. TPC operation achievements: temperature stability with double phase CO_2 cooling (left) and signal electron transparency with GEM gating (right).

adequately (Figure 5.23 left). For the second point an ion gating scheme based on GEM foils has been implemented and beam tested. Results show that a good transparency for drift electron signals can be maintained while preventing the accumulation of ions in the drift volume (Figure 5.23 right).

Jean Claude Brient, Wataru Ootani
3 pages

5.2.4 Electromagnetic Calorimeter

5.2.4.1 Silicon option

In the past 5 years the Silicon option of the electromagnetic calorimeter has focused on the design and construction of technological prototypes of the detector including beam tests. The current technological developments have led to choosing 20cm wafers for making the diode matrices, with a standard thickness of up to 725 micrometers. When applied to ILD this would result in a slightly thicker EM calorimeter than foreseen in the baseline design, and is one of the motivations to reduce the numbers of layers from 30 to 26 (see section 5.1.2).

A fully integrated layout of the detection board has been designed with the required dimension of 16 x 16 cm^2 corresponding to 1024 channels (Figure 5.24 top). The board hosts 16 SKIROC ASICs developed by OMEGA [ref] to process 64 channels each. A calorimeter prototype based on 10 such detection layers has been built (Figure 5.24 bottom) and beam-tested on several occasions at DESY and CERN, including a combined test with a SDHCAL prototype of the hadronic calorimeter (next section).

The response of this technological prototype to particles behaves as expected. A signal-to-noise ratio of 20 is measured for MIPs in single pads (Figure 5.25 left). Such a large signal/noise ratio of MIPs is important for isolated particle identification in particle flow energy reconstruction. First response to high energy electrons has recently been measured at CERN in a combined test with the SDHCAL (Figure 5.25 right). The beam tests have also been used to validate the power pulsing of the front-end electronics required to minimize heat production within the calorimeter. A new version

6.2.2 ILD Services and Utilities

Each component of ILD has requirements on services and utilities that are needed for operations and maintenance. This typically includes power and data lines, gas and cooling systems, guidances for laser beams, etc. All major support systems for those services, e.g. power supplies, cooling plants, lasers, DAQ computers, or gas systems are located outside of the detector, sometimes even far away (c.f. section 6.1.2.1). General paths have been defined in the global detector structure where space is allocated for those services. The routing of those paths has to be designed to minimise the amount of gaps and dead material in the active detector areas, while at the same time provide enough space for the foreseen utilities. Three main pathways have been defined for ILD:

1. The services of all barrel detectors are collected at the front-face of the barrel, go around the solenoid cryostat and leave the detector through the gap between the central yoke ring and the neighbouring rings.

2. The services of the endcap detectors (ECAL, HCAL, Muon) leave the detector along the endcap yoke ring.

3. The services for the forward calorimeter systems (FCAL, ECAL ring) pass parallel to the beamline, outside of the QD0 magnet.

This scheme allows for the opening of the yoke endcaps as well as for moving the barrel yoke rings independently from each other. The front-end electronic systems of the subdetectors can often drive only a limited cable length. Therefore, space for additional patch panels, drivers, data concentrators needs to be provided inside the ILD detector. While the exact requirements for those are not known in each case, conceptual locations have been defined. Figure 6.13 shows the general service paths and proposed locations for the patch panels in ILD.

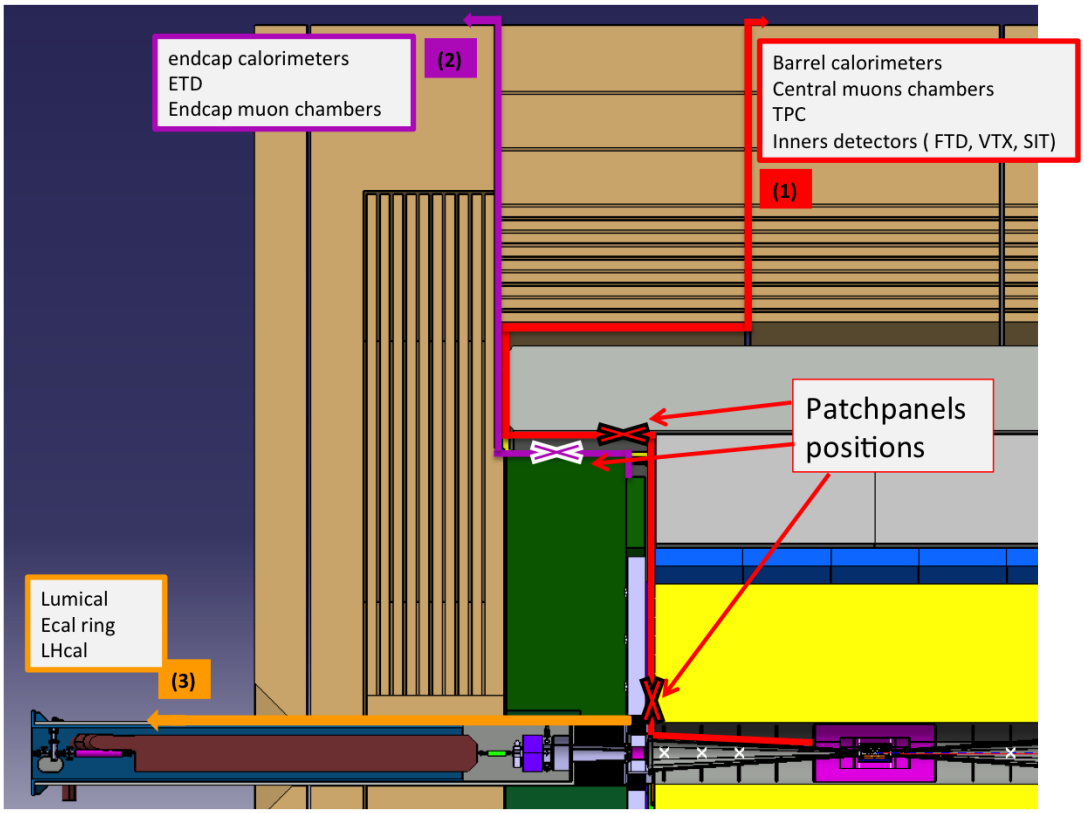

Figure 6.13. Service paths in the ILD detector and suggested positions for patch panels [2].

6.2.3 Inner Detector Integration

At the heart of ILD, directly at the interaction point, is the inner detector that comprises the beam pipe as well as the vertex detector and the intermediate silicon tracking devices, SIT and FTD (c.f. figure 6.14).

6.2.3.1 Mechanical Integration

The vertex detector is suspended from the beam pipe that itself is carried together with the Forward Tracking Disks and the Si Intermediate Tracker from the Inner Detector Support Structure (ISS). The ISS is a support tube made out of carbon-fibre reinforced plastic and is suspended from the end flanges of the TPC. A piezo-based active alignment system (see figure 6.15) allows for the positioning of the ISS with a precision better than 0.01 mm [47], independently of the main ILD detector structure. This is required to adjust the beam pipe and the inner tracking devices with respect to the beam axis, to better precision than what can be achieved with the complete ILD detector, e.g. after push-pull operations.

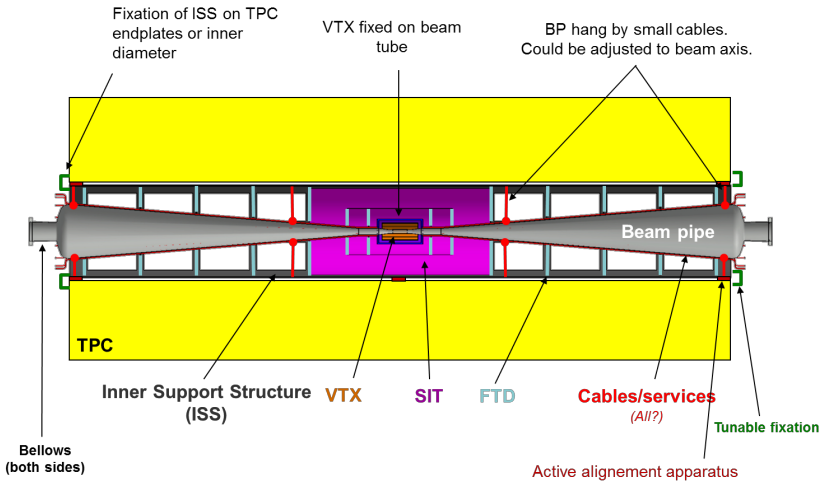

Figure 6.14. Schematic of the inner tracking detector system [47].

6.2.3.2 Electrical Services and Cooling

A rather detailed concept has been developed for the power scheme of the vertex detector (CMOS version), see figure 6.16. Copper based power and control cables as well as optical fibres for the data readout connect the vertex detector with patch panels at either ends of the ISS. From here, the cables are routed as described in section 6.2.2 to the outside of the detector. An engineering design for the details of the cabling and patch panels inside the ISS is still pending. Figure 6.17 shows the place holders for the cables in the current model. The vertex detector will be cooled using air flow cooling, where the cooling pipes also need to follow the general services paths.

6.2.4 TPC Integration

6.2.4.1 Mechanical integration

The mechanical integration of the TPC is still under study. Two possible concepts are being followed up. Either the TPC will be suspended directly from the solenoid cryostat with the help of carbon ribbons or support strats. Or it can be mounted to the absorber structure of the hadronic calorimeter.

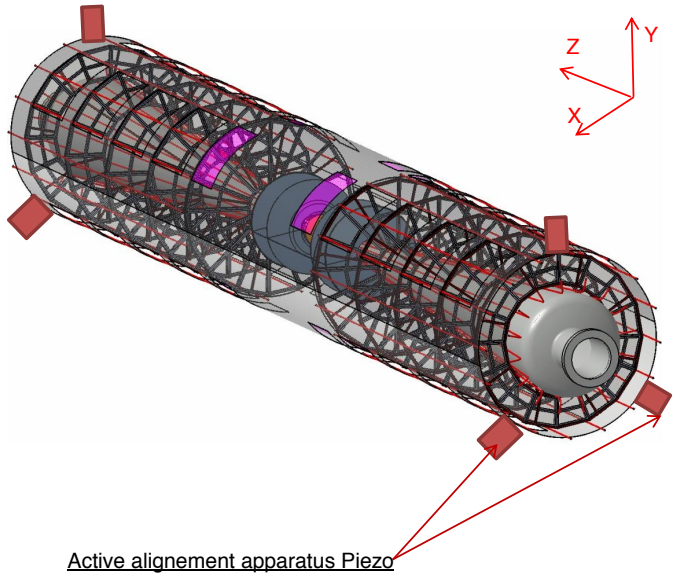

Figure 6.15. Engineering design of the inner detector [47].

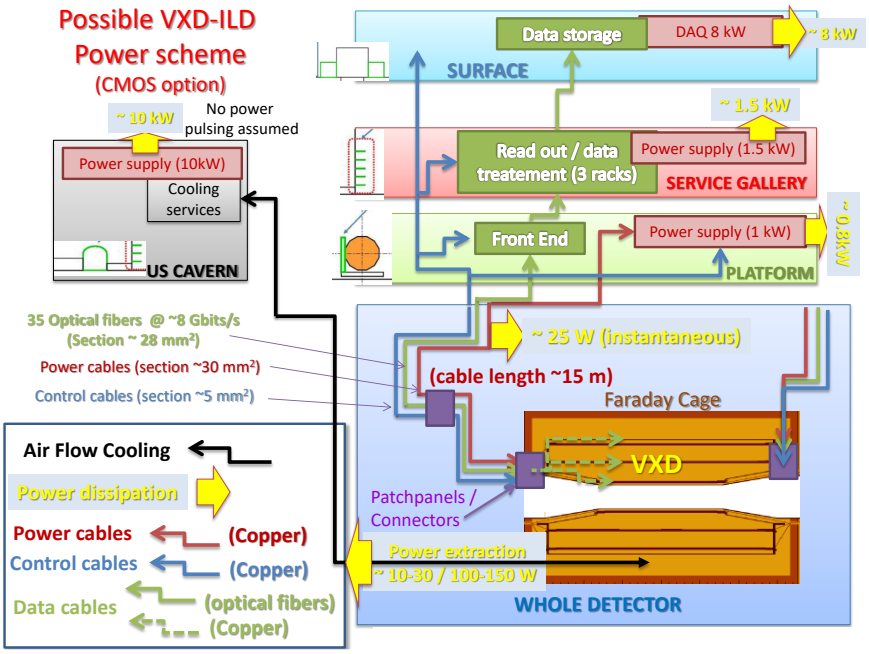

Figure 6.16. Diagram of a power scheme for the vertex detector (CMOS option) [48].

In the first case, the TPC would be decoupled from the mechanical properties of the calorimeters, at the price of having larger lever arms that might amplify vibrations. A longitudinal damping system would probably be required. In the second case, the lever arms would be much shorter, but the dynamic behaviour of the full system of the cryostat, hadronic and electomagnetic calorimeter as well as the TPC itself needs to be understood. Figure 6.18 shows the front face of the TPC, suspended from the hadronic calorimeter.

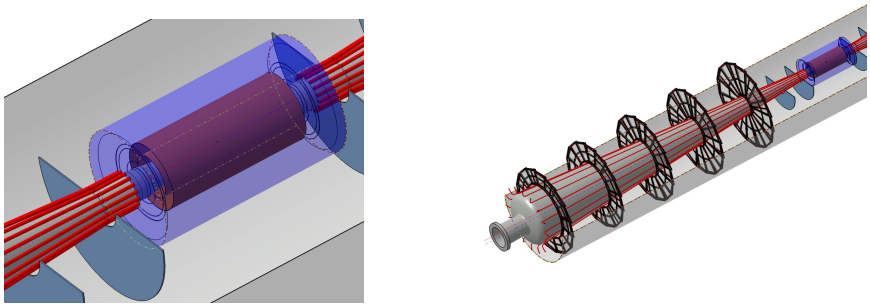

Figure 6.17. Cable placeholders for the inner SI detectors (VTX, SIT, FTD) [49].

6.2.4.2 Electrical Services and Cooling

The electrical services and the cooling pipes of the TPC start on both end plates and will be routed through gaps in the front-faces of the calorimeters, between the end-cap and barrel detectors (c.f. figure 6.18). A conceptual design for a cooling system, probably based on CO_2, is under development. Figure 6.19 shows a solution with a 6-loop geometry. The outer supplies of the TPC need to be accommodated in the detector environment. While a gas mixing and supply system will most probably be placed on the surface area, distribution sub-systems need to be closer to the detector, e.g. on the detector platform. The high-voltage power supplies will be place in the detector hall at reasonable cable lengths distance. Figure 6.20 shows a schematic drawing of the TPC connections to the outer world.

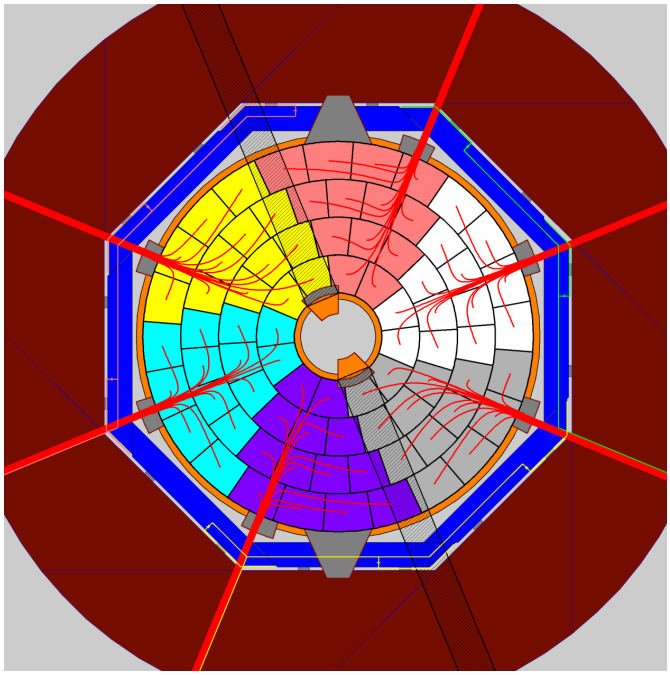

Figure 6.18. Conceptual design of the cable paths on the front-end of the TPC. The cables are routed to the outside in the marked gaps of the HCAL barrel electronics [50].

6.2.5 Electromagnetic Calorimeters Integration

6.2.5.1 Mechanical Integration

The two options under study for the ILD electromagnetic calorimeters, SiECAL and ScECAL, share the same mechanical design as shown in figure 5.7. The ECAL barrel consists of eight staves that

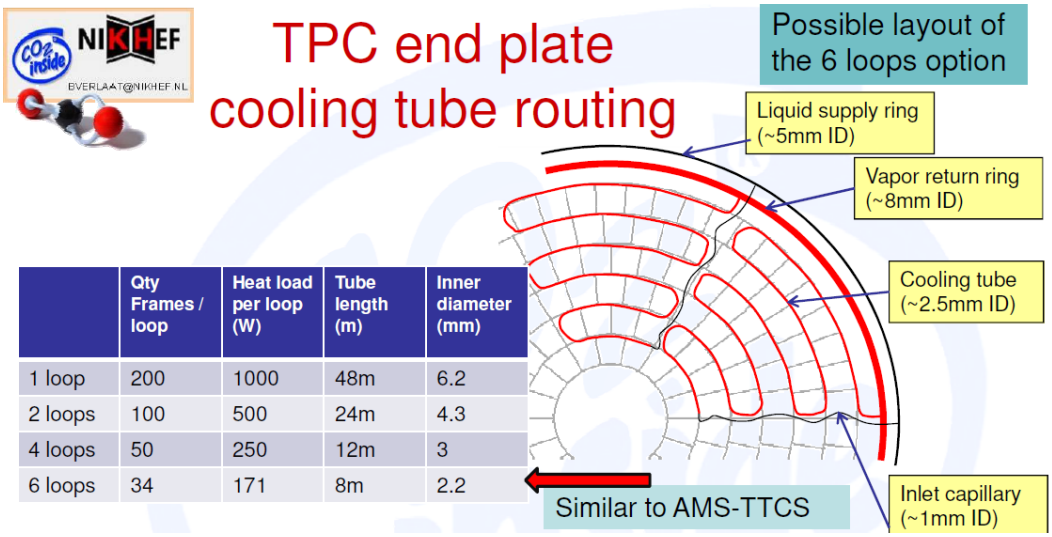

	Qty Frames / loop	Heat load per loop (W)	Tube length (m)	Inner diameter (mm)
1 loop	200	1000	48m	6.2
2 loops	100	500	24m	4.3
4 loops	50	250	12m	3
6 loops	34	171	8m	2.2

Figure 6.19. Options for the TPC cooling system with a conceptual design of the cooling tube routing on the TPC end plate [50].

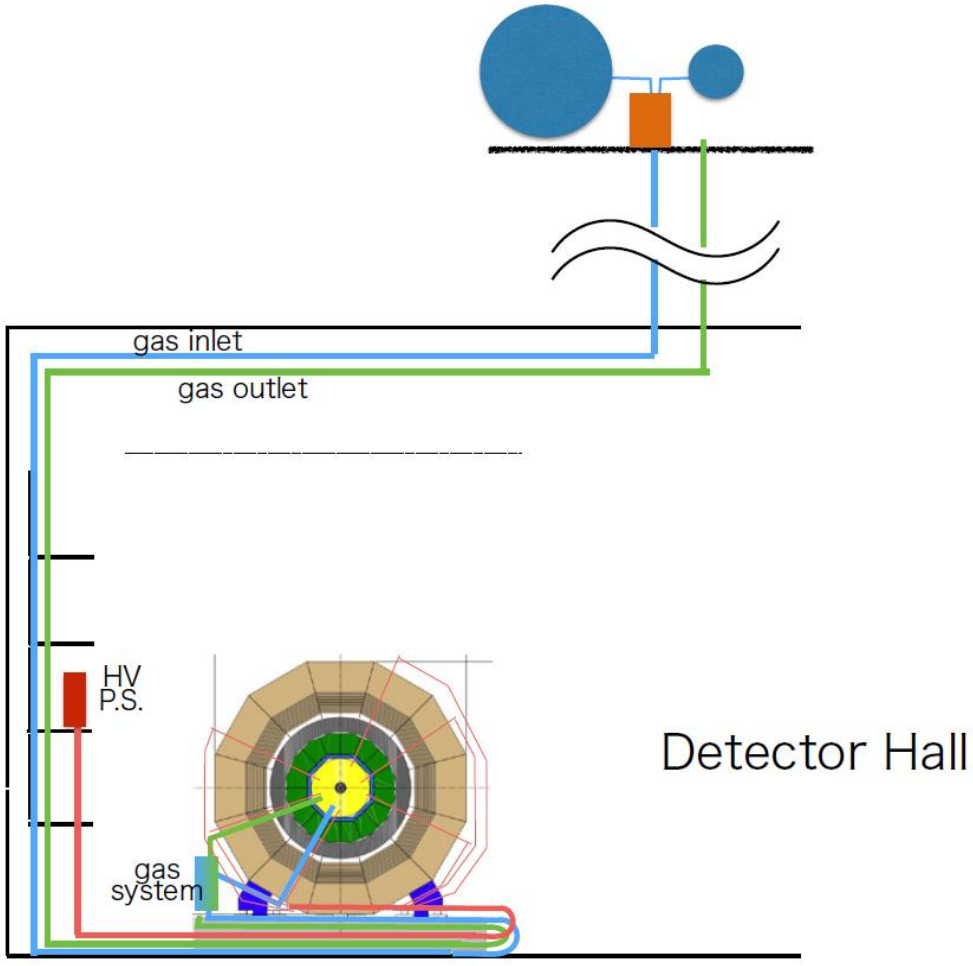

Figure 6.20. Gas and HC interfaces of the TPC [50].

are built from five modules each (c.f. figure 6.21). The staves are supported from the HCAL barrel sections. The ECAL endcaps are supported from the HCAL endcap detector.

Bibliography

[1] **ILD Concept Group**, T. Abe *et al.*, "The International Large Detector: Letter of Intent" arXiv:1006.3396 [hep-ex]. FERMILAB-LOI-2010-03, FERMILAB-PUB-09-682-E, DESY-2009-87, KEK-REPORT-2009-6.

[2] H. Abramowicz *et al.*, "The International Linear Collider Technical Design Report - Volume 4: Detectors" arXiv:1306.6329 [physics.ins-det].

[3] T. Barklow, J. Brau, K. Fujii, J. Gao, J. List, N. Walker, and K. Yokoya, "ILC Operating Scenarios" arXiv:1506.07830 [hep-ex].

[4] T. Behnke, J. E. Brau, B. Foster, J. Fuster, M. Harrison, J. M. Paterson, M. Peskin, M. Stanitzki, N. Walker, and H. Yamamoto, "The International Linear Collider Technical Design Report - Volume 1: Executive Summary" arXiv:1306.6327 [physics.acc-ph].

[5] P. Bambade *et al.*, "The International Linear Collider: A Global Project" arXiv:1903.01629 [hep-ex].

[6] M. Harrison, M. Ross, and N. Walker, "Luminosity Upgrades for ILC" in *Proceedings, 2013 Community Summer Study on the Future of U.S. Particle Physics: Snowmass on the Mississippi (CSS2013): Minneapolis, MN, USA, July 29-August 6, 2013*. 2013. arXiv:1308.3726 [physics.acc-ph].

[7] JAHEP, "A Proposal for a Phased Execution of the International Linear Collider Project ". http://www.jahep.org/office/doc/201210_ILC_staging_e.pdf.

[8] B. Warmbein, "The Road to Kitakami ". http://newsline.linearcollider.org/2014/02/20/the-road-to-kitakami/. ILC Newsline, 20. February 2014.

[9] B. Parker, A. Mikhailichenko, K. Buesser, J. Hauptman, T. Tauchi, P. Burrows, T. Markiewicz, M. Oriunno, and A. Seryi, "Functional Requirements on the Design of the Detectors and the Interaction Region of an Electron-Positron Linear Collider with a Push-Pull Arrangement of Detectors" in *Particle accelerator. Proceedings, 23rd Conference, PAC'09, Vancouver, Canada, May 4-8, 2009*, pp. WE6PFP078, ILC–Note–2009–050. 2010. http://www-public.slac.stanford.edu/sciDoc/docMeta.aspx?slacPubNumber=slac-pub-13657.

[10] **FCAL**, A. Levy, "The design of the ILD forward region" in *Proceedings, International Workshop on Future Linear Colliders 2016 (LCWS2016): Morioka, Iwate, Japan, December 05-09, 2016*. 2017. arXiv:1701.01923 [physics.ins-det].

[11] G. White, "BASELINE OPTICS TO PROVIDE FOR A SINGLE FFS L* (QD0 EXIT, IP DISTANCE) OPTICS CONFIGURATION". https://edmsdirect.desy.de/item/D00000001082495,A,1,1. ILC-CR-0002.

[12] R. Karl and J. List, "Impact of Beam-Gas Interactions in the IP Region of ILD ". https://confluence.desy.de/download/attachments/42357928/ILD-TECH-PUB-2017-001.pdf?version=1&modificationDate=1497399362316&api=v2. ILD-TECH-PUB-2017-001.

[13] **DEPFET**, O. Alonso *et al.*, "DEPFET active pixel detectors for a future linear e^+e^- collider" *IEEE Trans. Nucl. Sci.* **60** (2013) 1457, arXiv:1212.2160 [physics.ins-det].

[14] R. H. Richter *et al.*, "Design and technology of DEPFET pixel sensors for linear collider applications" *Nucl. Instrum. Meth.* **A511** (2003) 250–256.

[15] L. Andricek, G. Lutz, R. H. Richter, and M. Reiche, "Processing of ultra-thin silicon sensors for future e+ e- linear collider experiments" *IEEE Trans. Nucl. Sci.* **51** (2004) 1117–1120. [,667(2004)].

[16] L. Andricek *et al.*, "Intrinsic resolutions of DEPFET detector prototypes measured at beam tests" *Nucl. Instrum. Meth.* **A638** (2011) 24–32.

[17] J. J. Velthuis *et al.*, "A DEPFET based beam telescope with submicron precision capability" *IEEE Trans. Nucl. Sci.* **55** (2008) 662–666.

[18] C. Marinas and M. Vos, "The Belle-II DEPFET pixel detector: A step forward in vertexing in the superKEKB flavour factory" *Nucl. Instrum. Meth.* **A650** (2011) 59–63.

[19] **Belle-II**, T. Abe *et al.*, "Belle II Technical Design Report" arXiv:1011.0352 [physics.ins-det].

[20] G. Pellegrini *et al.*, "Technology developments and first measurements of low gain avalanche detectors (lgad) for high energy physics applications" *Nuclear Instruments and Methods A* **765** (2014) 12 – 16. http://www.sciencedirect.com/science/article/pii/S0168900214007128.

[21] M. Carulla *et al.*, "Technology developments and first measurements on inverse low gain avalanche detector (iLGAD) for high energy physics applications"*Journal of Instrumentation* **11** (dec, 2016) C12039–C12039. https://doi.org/10.1088%2F1748-0221%2F11%2F12%2Fc12039.

[22] E. Currás, A. García, M. Centis Vignali, J. González, S. Hidalgo, M. Carulla, A. Merlos, D. Flores, J. Duarte-Campderros, G. Pellegrini, *et al.*, "arxiv: Inverse low gain avalanche detectors (ilgads) for precise tracking and timing applications" tech. rep., 2019.

[23] **LCTPC**. https://www.lctpc.org.

[24] R. Diener *et al.*, "The desy ii test beam facility" *Nucl. Instrum. Meth.* **A922** (2019) 265–286.

[25] M. Wu *et al.*, "Development of a large active area beam telescope based on the sid micro-strip sensor". http://cds.cern.ch/record/2666439. Poster presented at Vienna Conference of Instrumentation 2019.

[26] **LCTPC**, "talks".

[27] C. Ligtenberg *et al.*, "Performance of a gridpix detector based on the timepix3 chip" *Nucl. Instrum. Meth.* **A908** (2018) 18–23.

[28] L. Raux *et al.*, "SPIROC (SiPM Integrated Read-Out Chip): Dedicated very front-end electronics for an ILC prototype hadronic calorimeter with SiPM read-out" *JINST* **6** (2011) C01098.

[29] **CALICE Collaboration**, C. Adloff *et al.*, "Hadronic energy resolution of a highly granular scintillator-steel hadron calorimeter using software compensation techniques" *JINST* **7** (2012) P09017, arXiv:1207.4210 [physics.ins-det]. MPP-2012-116.

[30] **CALICE**, C. Adloff *et al.*, "Track segments in hadronic showers in a highly granular scintillator-steel hadron calorimeter" *JINST* **8** (2013) P09001, arXiv:1305.7027 [physics.ins-det].

[31] **CALICE**, C. Adloff *et al.*, "Validation of GEANT4 Monte Carlo Models with a Highly Granular Scintillator-Steel Hadron Calorimeter" *JINST* **8** (2013) 07005, arXiv:1306.3037 [physics.ins-det].

[32] **CALICE**, C. Adloff *et al.*, "Shower development of particles with momenta from 1 to 10 GeV in the CALICE Scintillator-Tungsten HCAL" *JINST* **9** (2014) no. 01, P01004, arXiv:1311.3505 [physics.ins-det].

[33] **CALICE**, C. Adloff *et al.*, "The Time Structure of Hadronic Showers in highly granular Calorimeters with Tungsten and Steel Absorbers" *JINST* **9** (2014) P07022, arXiv:1404.6454 [physics.ins-det].

[34] **CALICE**, B. Bilki *et al.*, "Pion and proton showers in the CALICE scintillator-steel analogue hadron calorimeter" *JINST* **10** (2015) no. 04, P04014, arXiv:1412.2653 [physics.ins-det].

[35] **CALICE**, M. Chefdeville *et al.*, "Shower development of particles with momenta from 15 GeV to 150 GeV in the CALICE scintillator-tungsten hadronic calorimeter" *JINST* **10** (2015) no. 12, P12006, arXiv:1509.00617 [physics.ins-det].

[36] **CALICE**, G. Eigen *et al.*, "Hadron shower decomposition in the highly granular CALICE analogue hadron calorimeter" *JINST* **11** (2016) no. 06, P06013, arXiv:1602.08578 [physics.ins-det].

[37] **CALICE**, J. Repond *et al.*, "Hadronic Energy Resolution of a Combined High Granularity Scintillator Calorimeter System" *JINST* **13** (2018) no. 12, P12022, arXiv:1809.03909 [physics.ins-det].

[38] O. Hartbrich, *Scintillator Calorimeters for a Future Linear Collider Experiment*. PhD thesis, Hasylab, DESY, Hamburg, 2016. http://bib-pubdb1.desy.de/search?cc=Publication+Database&of=hd&p=reportnumber:DESY-THESIS-2016-020.

[39] G. Blazey, D. Chakraborty, A. Dyshkant, K. Francis, D. Hedin, *et al.*, "Directly coupled tiles as elements of a scintillator calorimeter with MPPC readout" *Nucl.Instrum.Meth.* **A605** (2009) 277–281. FERMILAB-PUB-09-585-E.

[40] F. Simon and C. Soldner, "Uniformity Studies of Scintillator Tiles directly coupled to SiPMs for Imaging Calorimetry" *Nucl.Instrum.Meth.* **A620** (2010) 196–201, arXiv:1001.4665 [physics.ins-det]. MPP-2010-10.

[41] H. Hayano, "Kitakami Site-specific CFS Study Update". https://agenda.linearcollider.org/event/7645/. International Workshop on Future Linear Colliders LCWS2017, Strasbourg, October 2017.

[42] M. Miyahara, "Update on Detector Hall and Assembly Hall Layout". http://https://agenda.linearcollider.org/event/6910/. Mini-Workshop on Infrastructure and CFS for Physics and Detectors, KEK, March 2016.

[43] M. Miyahara, "Update on Detector Hall and Assembly Hall Design". https://agenda.linearcollider.org/event/6851/. Mini-Workshop on Infrastructure and CFS for Physics and Detectors, KEK, September 2015.

[44] Y. Sugimoto, "Detector Utility". https://agenda.linearcollider.org/event/8123/. Mini-Workshop on Infrastructure and CFS for Physics and Detectors, KEK, February 2019.

[45] K. Buesser and T. Schoerner-Sadenius, "MDIPlan, E-JADE Deliverable Report 22". https://www.e-jade.eu/sites/sites_custom/site_e-jade/content/e49893/e65922/e84403/D.22.WP3.MDI.v3.pdf. E-Jade.Deliverable.WP3.D22.MDIPlan.v3.

[46] M. Oriunno, "SiD Underground Assembly". https://agenda.linearcollider.org/event/6404/. MDI-CFS Meeting on ILC Interaction Region Issues, Ichinoseki, September 2014.

[47] A. Gonnin and C. Bourgeois, "Integration of the inner detector region". https://edmsdirect.desy.de/item/D00000001003815,A,1,1. EDMS ID: D00000001003815,A,1,1.

[48] A. Besson, "VTX and Intermediate Tracking Status". https://agenda.linearcollider.org/event/8126/. ILD Integration Meeting, DESY, February 2019.

[49] A. Gonnin and R. Poeschl, "ILD Cabling - what we know today". https://agenda.linearcollider.org/event/8126/. ILD Integration Meeting, DESY, February 2019.

[50] P. Colas *et al.*, "TPC Interface Control Document". https://edmsdirect.desy.de/item/D00000001162555,A,1,1. EDMS ID: D00000001162555,A,1,1.

[51] R. Poeschl and H. Videau, "VFS Interface Control Document". https://edmsdirect.desy.de/item/D00000001162465,A,1,1. EDMS-ID: D00000001162465,A,1,1.

[52] T. Takeshita, "ScECAL Interface Control Document". https://edmsdirect.desy.de/item/D00000001162515,A,1,1. EDMS-ID: D00000001162515,A,1,1.

[53] S. Schuwalow and Y. Benhammou, "VFS Interface Control Document". https://edmsdirect.desy.de/item/D00000001163265,A,1,1. EDMS-ID: D00000001163265,A,1,1.

[54] M. Wing *et al.*, "Common DAQ system ready for combined tests, AIDA-2020 report, AIDA-2020-MS80 (2018)". http://cds.cern.ch/record/2314260.

[55] F. Kircher *et al.*, "Conceptual Design of the ILD Detector Magnet System". http://flc.desy.de/lcnotes/notes/localfsExplorer_read?currentPath=/afs/desy.de/group/flc/lcnotes/LC-DET-2012-081.pdf. LC-DET-2012-081.

[56] R. Stromhagen, "Note on the integration of Cryostat into the Central Barrel - ILD Detector ". https://edmsdirect.desy.de/item/D00000001010065,A,1,1. EDMS-ID: D00000001162515,A,1,1.

[57] A. Seryi, T. Maruyama, and B. Parker, "IR Optimization, DID and anti-DID". SLAC-PUB-11662.

[58] Y. Makida *et al.*, "Interim Report from Toshiba/Hitachi Studies on Solenoid and Anti-DID ". https://agenda.linearcollider.org/event/7520. ILD Software and Technical Meeting, Lyon, April 2017.

[59] U. Schneekloth, "ILD Magnet Activities ". https://agenda.linearcollider.org/event/7760/. ILD Meeting, Ichinoseki, February 2018.

[60] T. Sanami *et al.*, "IR Hall Dose Rate Estimates with Detector Concepts ". SLAC Radiation Physics Note, RP-09-08.

[61] "High Sensitivity Seismograph Network Japan". http://www.hinet.bosai.go.jp.

[62] T. Tauchi, "Standard Reference Earthquake Parameters". https://edmsdirect.desy.de/item/D00000001164345,A,1,1. ILC-EDMS D*1164345.

[63] T. Sanuki *et al.*, "Seismic Isolation ". https://agenda.linearcollider.org/event/7976/. Mini-Workshop on ILC Infrastructure and CFS for Physics and Detectors, KEK, Tsukuba, November 2018.

[64] "ILC Engineering Data Management System". https://ilc-edms.desy.de.

[65] "ILD Technical Documentation". https://edmsdirect.desy.de/treebrowser/ildtdr/.

[66] iLCSoft authors, "iLCSoft Project Page". https://github.com/iLCSoft, 2016.

[67] W. Kilian, T. Ohl, and J. Reuter, "WHIZARD: Simulating Multi-Particle Processes at LHC and ILC" *Eur. Phys. J.* **C71** (2011) 1742, arXiv:0708.4233 [hep-ph].

[68] T. Sjostrand, S. Mrenna, and P. Z. Skands, "PYTHIA 6.4 Physics and Manual" *JHEP* **05** (2006) 026, arXiv:hep-ph/0603175 [hep-ph].

[69] D. Schulte, "Beam-beam simulations with Guinea-Pig" *eConf* **C980914** (1998) 127–131. [,127(1998)].

[70] P. Chen, T. L. Barklow, and M. E. Peskin, "Hadron production in gamma gamma collisions as a background for e+ e- linear colliders" *Phys. Rev.* **D49** (1994) 3209–3227, arXiv:hep-ph/9305247 [hep-ph].

[71] F. Gaede, T. Behnke, N. Graf, and T. Johnson, "LCIO: A Persistency framework for linear collider simulation studies" *eConf* **C0303241** (2003) TUKT001, arXiv:physics/0306114 [physics].

[72] F. Gaede, "Marlin and LCCD: Software tools for the ILC" *Nucl. Instrum. Meth.* **A559** (2006) 177–180.

[73] M. Frank, F. Gaede, C. Grefe, and P. Mato, "DD4hep: A Detector Description Toolkit for High Energy Physics Experiments" *J. Phys. Conf. Ser.* **513** (2014) 022010.

[74] M. Frank, F. Gaede, N. Nikiforou, M. Petric, and A. Sailer, "DDG4 A Simulation Framework based on the DD4hep Detector Description Toolkit" *J. Phys. Conf. Ser.* **664** (2015) no. 7, 072017.

[75] **GEANT4**, S. Agostinelli *et al.*, "GEANT4: A Simulation toolkit" *Nucl. Instrum. Meth.* **A506** (2003) 250–303.

[76] lcgeo authors, "lcgeo Project Page". `https://github.com/iLCSoft/lcgeo`, 2016.

[77] F. Gaede, S. Aplin, R. Glattauer, C. Rosemann, and G. Voutsinas, "Track reconstruction at the ILC: the ILD tracking software" *J. Phys. Conf. Ser.* **513** (2014) 022011.

[78] J. S. Marshall and M. A. Thomson, "The Pandora Software Development Kit for Pattern Recognition" *Eur. Phys. J.* **C75** (2015) no. 9, 439, `arXiv:1506.05348 [physics.data-an]`.

[79] T. Suehara and T. Tanabe, "LCFIPlus: A Framework for Jet Analysis in Linear Collider Studies" *Nucl. Instrum. Meth.* **A808** (2016) 109–116, `arXiv:1506.08371 [physics.ins-det]`.

[80] M. Cacciari, "FastJet: A Code for fast k_t clustering, and more" in *Deep inelastic scattering. Proceedings, 14th International Workshop, DIS 2006, Tsukuba, Japan, April 20-24, 2006*, pp. 487–490. 2006. `arXiv:hep-ph/0607071 [hep-ph]`. [,125(2006)].

[81] **CLIC detector, physics study**, C. Grefe, S. Poss, A. Sailer, and A. Tsaregorodtsev, "ILCDIRAC, a DIRAC extension for the Linear Collider community" *J. Phys. Conf. Ser.* **513** (2014) 032077.

[82] A. Miyamoto and H. Ono, "ILD MC production for detector optimization" in *International Workshop on Future Linear Colliders (LCWS 2018) Arlington, Texas, USA, October 22-26, 2018*. 2019. `arXiv:1902.02516 [physics.ins-det]`.

[83] M. Berggren, "SGV 3.0 - a fast detector simulation" in *International Workshop on Future Linear Colliders (LCWS11) Granada, Spain, September 26-30, 2011*. 2012. `arXiv:1203.0217 [physics.ins-det]`.

[84] M. Kurata and R. Yonamine, "Higgs branching ratio study for new detector models as benchmark process in ILD". `https://confluence.desy.de/display/ILD/ILD+notes`, 2019.

[85] F. J. Mueller, *Development of a Triple GEM Readout Module for a Time Projection Chamber & Measurement Accuracies of Hadronic Higgs Branching Fractions in $\nu\nu$H at a 350 GeV ILC*. PhD thesis, DESY, Hamburg, 2016. `http://bib-pubdb1.desy.de/search?cc=Publication+Database&of=hd&p=reportnumber:DESY-THESIS-2016-018`.

[86] H. Ono, "Higgs branching ratio study for DBD detector benchmarking in ILD" in *Helmholtz Alliance Linear Collider Forum: Proceedings of the Workshops Hamburg, Munich, Hamburg 2010-2012, Germany*, pp. 203–223, DESY. DESY, Hamburg, 2013.

[87] H. Ono and A. Miyamoto, "A study of measurement precision of the Higgs boson branching ratios at the International Linear Collider" *Eur. Phys. J.* **C73** (2013) no. 3, 2343, `arXiv:1207.0300 [hep-ex]`.

[88] J. Yan, S. Watanuki, K. Fujii, A. Ishikawa, D. Jeans, J. Strube, J. Tian, and H. Yamamoto, "Measurement of the Higgs boson mass and $e^+e^- \to ZH$ cross section using $Z \to \mu^+\mu^-$ and $Z \to e^+e^-$ at the ILC" *Phys. Rev.* **D94** (2016) no. 11, 113002, `arXiv:1604.07524 [hep-ex]`.

[89] J. Tian, "Higgs Mass Measurement at $\sqrt{s} = 500\,\text{GeV}$ as benchmark process in ILD". https://confluence.desy.de/display/ILD/ILD+notes, 2019.

[90] S. Kawada, "Branching ratio $H \to \mu^+\mu^-$ at $\sqrt{s} = 500\,\text{GeV}$ as benchmark process in ILD". https://confluence.desy.de/display/ILD/ILD+notes, 2019.

[91] Y. Kato, "$H \to$ invisible at $\sqrt{s} = 500\,\text{GeV}$ as benchmark process in ILD". https://confluence.desy.de/display/ILD/ILD+notes, 2019.

[92] M. Boronat, J. Fuster, I. Garcia, E. Ros, and M. Vos, "A robust jet reconstruction algorithm for high-energy lepton colliders" *Phys. Lett.* **B750** (2015) 95–99, arXiv:1404.4294 [hep-ex].

[93] D. Jeans and K. Yumino, "τ polarisation in $e^+e^- \to \tau^+\tau^-$ at $\sqrt{s} = 500\,\text{GeV}$ as benchmark process in ILD". https://confluence.desy.de/display/ILD/ILD+notes, 2019.

[94] J. Beyer, "Vector Boson Scatering at $\sqrt{s} = 1\,\text{TeV}$ as benchmark process in ILD". https://confluence.desy.de/display/ILD/ILD+notes, 2019.

[95] T. Mizuno, "Calibration of the photon energy scale from $e^+e^- \to \gamma\mu^+\mu^-$ as benchmark process in ILD". https://confluence.desy.de/display/ILD/ILD+notes, 2019.

[96] A. Irles and Y. Okugawa, "$e^+e^- \to b\bar{b}$ and $e^+e^- \to t\bar{t}$ as benchmark processes in ILD". https://confluence.desy.de/display/ILD/ILD+notes, 2019.